

Effects of Mn Additions on the Structure, Mechanical Properties, and Corrosion Behavior of Cu-Al-Ni Shape Memory Alloys

Safaa N. Saud, E. Hamzah, T. Abubakar, H.R. Bakhsheshi-Rad, Mohd Zamri, and Masaki Tanemura

(Submitted April 3, 2014; in revised form May 22, 2014; published online July 8, 2014)

The influences of different amount (0.4, 0.7, and 1 wt.%) of Mn addition on the structure, mechanical properties, and corrosion behavior of Cu-Al-Ni shape memory alloys have been studied using differential scanning calorimetry, field emission scanning electron microscopy, transmission electron microscopy, x-ray diffraction, tensile test, shape memory effect test, hardness test, and electrochemical test. It was observed that the transformation temperatures, microstructural characteristics, and mechanical properties are highly sensitive to the composition variations. The obtained results show that the transformation temperatures and mechanical properties of Cu-Al-Ni SMAs exhibited the best results with 0.7 wt.% of Mn addition. These kinds of enhancements are mainly due to the type, amount, and morphology of the martensite phase, including the grain refinement. The result of electrochemical test showed that an increment in Mn content up to 0.7 wt.% improved the corrosion resistance of Cu-Al-Ni SMA. However, further increase of Mn content decreases the corrosion resistance of the alloy.

Keywords corrosion, martensitic transformation, microalloying, shape memory alloys, shape memory effects

1. Introduction

Cu-based shape memory alloys (SMAs) have attracted lots of interests from scientists and researchers in order to be utilized in many practical applications (Ref 1), due to their wide-ranging transformation temperatures, inexpensive, and easy to produce. Among the Cu-based alloys, Cu-Al-Ni SMAs are the most used alloys, and in particular whenever high temperatures are required. Therefore, they are assigned to their high transformation temperatures that are able to work at near to 200 °C (Ref 2), which are usually difficult for Cu-Zn-Al, Cu-Al-Be, Cu-Al-Mn, and NiTi alloys (Ref 3-6), whose maximum temperatures are around 100 °C (Ref 7). The shape memory effect of these alloys is able to display at a specific composition of about 11-14 wt.% for aluminum and 3-5 wt.% for nickel. Additionally, to control/slow down the diffusivity of Cu and Al, nickel was added. However, this addition may result in suppressing the decompo-

sition of the β -phase during the cooling process (Ref 8). There are some ordered structures formed from the transformation of A2 type disordered in the Cu-based SMAs during the quenching process from high temperatures. Further cooling may transfer these types of ordered structures into various well-known structures, namely, 6R, 18R, and 2H; where the R and H refer to rhombohedral and hexagonal structures, respectively. For Cu-Al-Ni SMAs, two martensite structures typically produced are, 2H (γ'_1) and 18R (β'_1), which are thermally induced martensite (Ref 9). The formation of these structures is affected by Al and Ni compositions, along with the heat treatment. Throughout the cooling treatment, and also at a low content of Al, the martensite formed is β'_1 , while γ'_1 is formed at an elevated amount of Al. Each of these structures has a different transformation feature, and the difference between their hysteresis temperatures is about 20 °C (Ref 10-12). From this perspective, the amount of Al in these types of alloys has a considerable influence on the structure, along with effects on the properties. While Cu-Al-Ni SMAs have a high transformation temperature and better thermal stability, their applications are limited as a consequence of their low workability and is expected to produce a brittle intergranular crack (Ref 13), which could be a result of an extreme elastic anisotropy and large grain size. Consequently, the mechanical properties are reduced, and contribute to form a higher order degree in the parent phase with a different structure (B2, Do₃, and/or L2₁). To overcome the problems, two ways have been identified by several researchers: (a) adding the alloying elements and (b) heat treatment (Ref 14-18), by which they are able to control grain size and consequently having an effect on the mechanical properties (Ref 7, 19). Adachi (Ref 20) revealed that the Ti-doped in Cu-Al-Ni SMA reduced the grain size and leads to enhancing the mechanical properties, while Morris (Ref 15) refers in his study to the fact that the addition of boron and zirconium can lead to an improvement in the mechanical properties.

Safaa N. Saud, E. Hamzah, T. Abubakar, and H.R. Bakhsheshi-Rad, Faculty of Mechanical Engineering, Universiti Teknologi Malaysia, 81310 UTM Johor Bahru, Johor, Malaysia; Mohd Zamri, Faculty of Mechanical Engineering, Universiti Teknologi Malaysia, 81310 UTM Johor Bahru, Johor, Malaysia and Department of Frontier Materials, Nagoya Institute of Technology, Gokiso-cho, Showa-ku, Nagoya 466-8555, Japan; and Masaki Tanemura, Department of Frontier Materials, Nagoya Institute of Technology, Gokiso-cho, Showa-ku, Nagoya 466-8555, Japan. Contact e-mails: safaaengineer@gmail.com and esah@fkm.utm.my.

In this paper, various additions of Mn were added to investigate their effects on the microstructures, mechanical properties, and corrosion characteristic of Cu-11.9 wt.% Al-4 wt.% Ni SMA. The materials were characterized by using a differential scanning calorimeter (DSC), field emission scanning electron microscopy (FESEM), transmission electron microscopy (TEM), energy dispersive spectroscopy (EDS), and x-ray diffraction (XRD) analysis. Mechanical tests were performed on the materials included a tensile test, a shape memory test, Vicker's hardness test, and electrochemical test.

2. Materials and Methods

2.1 Materials Preparation

The alloys were produced by melting the high purity metals of Cu, Al, Ni, and Mn, using an induction furnace. These metals were melted in a silicon carbide crucible at a temperature of about 1300 °C with continuous stirring and were then poured into a cast iron mold with dimensions of 270 mm × 50 mm × 20 mm. The ingot was cut into the required sample dimensions using Electrical discharge machining wire (EDM) and then homogenized at 900 °C for 30 min, followed by quenching in water, which led to the formation of martensite. The chemical composition analysis for the as-cast Cu-Al-Ni-xMn SMAs ($x = 0, 0.4, 0.7, 1$ wt.%) was investigated using inductively coupled plasma mass spectrometry (ICP-MS). These results are shown in Table 1.

2.2 Materials Characterization

Flat specimens were cut from the samples with dimensions of 10 mm × 10 mm × 2 mm for the microstructural (FE-SEM and EDS) and XRD characteristics. TEM (a JEM2010 operated at 200 kV) was also used to investigate the microstructural changes. Filings of the alloys removed were about 2-6 mg and were taken for the DSC measurements (a Mettler Toledo DSC 822e) with a scanning rate of 10 °C/min within the 50-300 °C range. The phase identifications and crystal structure determinations were carried out using a D5000 Siemens x-ray diffractometer fitted with a CuK α x-ray source with a locked couple mode, a 2 θ range of between 30° and 60°, and a 0.05°/s scanning step. The quenched samples were ground and polished, then etched in a solution containing 2.5 g ferric chloride (FeCl₃·6H₂O) and 48 mL methanol (CH₃OH) in 10 mL HCl for 4 min (Ref 10, 21, 22).

2.3 Mechanical Tests

2.3.1 Tensile and Hardness Tests. The tensile test was performed using an Instron 5982-type universal testing machine operated at a constant strain rate of 0.1 mm/min.

Table 1 Chemical compositions of the alloys (mass fraction, wt.%)

Alloy	Cu	Al	Ni	Mn
1	84.1	11.9	4	...
2	83.7	11.9	4	0.4
3	83.4	11.9	4	0.7
4	83.1	11.9	4	1

The tests were carried out at room temperature until a failure. The fracture stress-strain was determined under the tensile load, and the fracture surface was examined using Scanning electron microscopy (SEM). The purpose of this test was to determine the elastic and plastic region before performing the shape memory effect test. Vicker's microhardness test with 10 kg for 25 s was performed to measure the hardness of these alloys.

2.3.2 Shape Memory Effect Test. The shape memory effect test was carried out using a specially designed machine, which consists of an Instron 5982-type universal testing machine, equipped with a heater tape and digital thermocouple to control the applied temperature, as well as an external extensometer to measure the shape extension and recovery. The tests were carried out at a temperature below A_s (austenite start temperature), which was about 100 °C, where the alloys would be able to obtain shape recovery. Then, the deformed sample that still had an unrecoverable shape was subsequently heated above the austenite finish temperature ($A_f + 60$ °C) for 10 min, followed by water quench to recover the residual strain (ϵ_r). The recovered shape was attributed to the transformation of the detwinned martensite to the austenite phase, which had been termed as a transformation strain (ϵ^t). After the cooling process, the martensite was again formed into a self-accommodated structure.

2.3.3 Electrochemical Test. Rectangular specimens with a surface area of 1 cm² were molded into epoxy resin for electrochemical tests. The test was conducted at 20 °C in the open air in a glass cell containing 350 ml of 3.5% NaCl solution by using a PARSTAT 2263 potentiostat/galvanostat (Princeton Applied Research). A three-electrode cell was used for potentiodynamic polarization tests, where the reference electrode was a saturated calomel electrode (SCE), the counter electrode was made of graphite rod, and the specimen was the working electrode. All experiments were carried out at a constant scan rate of 0.5 mV/s initiated at -250 mV_{SCE} below the open circuit potential. This fitting is inherently difficult, but the software has the ability to allow manual control. Tafel fittings were generally carried out by selecting a segment of the curve from E_{corr} V_{SCE}, and i_{corr} was subsequently estimated from the value where the fit intercepted the potential value of the true E_{corr} V_{SCE} (Ref 23). Each experiment was repeated twice to check the reproducibility of the results. All potentials were referred to the SCE.

3. Results and Discussion

3.1 Transformation Temperatures

The phase transformation characteristics of the Cu-Al-Ni SMAs with and without Mn addition have been determined by DSC, and the data are tabulated in Table 2. Figure 1 shows the DSC heating and cooling curves of the alloys, whereas the results of both curves are not statistically verified. The forward transformation curve exhibited a single peak that refers to the martensite-austenite transformation. While, the backward transformation curve exhibited multi-peaks, which starts with a very smooth low temperature peak, then followed by a high temperature peak. These multi-peaks are due to the interface transformation. On the other hand, the DSC curves obtained for alloys with the Mn addition, the transformation temperatures were shifted toward high temperatures and reached to the maximum values for 0.7 wt.% Mn alloy.

However, higher amount of Mn, i.e., around 1 wt.%, leads to decrease in the transformation temperatures. The transformation temperature variation is mainly attributed to the type and morphology of the martensite phase, as well as the order and stabilizes degree of γ'_1 (Ref 21). Based on these results, it has been proven that the Mn additions have strong influences on the transformation temperatures of Cu-Al-Ni SMA, and these influences are due to the high sensitivity of these alloys to the changes in the alloying compositions.

Based on the thermodynamic calculation, the equilibrium temperature, T_o , between the parent phase and martensite phase is obtained when the Gibbs free energy (G) of both phases are equalized. Based on the following relations, the T_o was calculated as

$$\begin{aligned} \Delta G^{M \rightarrow A}(T_o) &= G^A(T_o) - G^M(T_o) = (H^A - T_o S^A) \\ &\quad - (H^M - T_o S^M) = \Delta H^{M \rightarrow A} - T_o \Delta S^{M \rightarrow A} \end{aligned} \quad (\text{Eq 1})$$

Or

$$\begin{aligned} \Delta G^{A \rightarrow M}(T_o) &= G^M(T_o) - G^A(T_o) = (H^M - T_o S^M) \\ &\quad - (H^A - T_o S^A) = \Delta H^{A \rightarrow M} - T_o \Delta S^{A \rightarrow M} \end{aligned} \quad (\text{Eq 2})$$

In addition to T_o for the alloy, when the $\Delta G^{M \rightarrow A}(T_o)$ and $\Delta G^{A \rightarrow M}(T_o) = 0$ at $T = T_o$ is expressed as (Ref 24, 25)

$$T_o = \frac{\Delta H^{M \rightarrow A}}{\Delta S^{M \rightarrow A}} \quad \text{or} \quad T_o = \frac{\Delta H^{A \rightarrow M}}{\Delta S^{A \rightarrow M}} \quad (\text{Eq 3})$$

The equilibrium temperature between the austenite and martensite phase transformation can be expressed as

$$T_o = \frac{1}{2}(M_s + A_f) \quad (\text{Eq 4})$$

The T_o is calculated before and after the addition and tabulated in Table 2. It was found that the maximum value of T_o was observed with Cu-Al-Ni-0.7 wt.% Mn. Moreover, the thermodynamic parameters of forward and reverse transformation are calculated and indicated in Table 3. The enthalpy (ΔH) and entropy (ΔS) of both transformations are tending to decreased with increasing the amount of Mn. As the thermal stability is inversely proportional to the enthalpy, it was found that the higher martensite thermal stability is obtained with Cu-Al-Ni-1wt. % Mn, which may relate to the amount of precipitates, behavior, and the morphology of the martensite phase.

3.2 Microstructural Changes

In order to investigate the effect of Mn addition on the microstructural characteristics, FESEM and TEM were used.

Figure 2(a)-(d) shows the micrographs of Cu-Al-Ni SMAs with and without the addition of Mn. It was found that all the microstructures obtained are in martensite state at the room temperature with two different morphologies: needles and plates. These morphologies are referred to as two types of thermal induced martensite: β'_1 and γ'_1 phases, whereas the γ'_1 formed as a coarse variants/plates, while the β'_1 formed as a small needles between the γ'_1 plates. The small needles of the β'_1 martensite have very high thermoelastic behavior, which can be attributed to their controlled growth in the self-accommodating groups. However, the micrographs showed a self-accommodation martensite plates, whereas the nucleation and growing of these plates were performed at different sites. The growth process of the martensite involves the accommodation of the local stress field, which requires formation of other plates groups (Ref 21). On the other hand, the orientations and the thickness of the needles and plates groups varied in accordance to the Mn percentage additions, whereas the thickness of γ'_1 plates is gradually increased after Mn is added. The orientations of the martensite plates group are parallel both horizontal and vertical. The average grain size exhibits a significant difference among the alloys, whereas the grain size of the base alloy (Cu-Al-Ni) was around 1400 μm and decreases to 600, 300, and 450 μm for 0.4, 0.7, and 1 wt.% Mn, respectively. In other words, the grain size decreased to about 80% due to the Mn addition. Others researchers have shown that the grain size of the Cu-Al-Ni SMA can vary between 1 and 3 μm (Ref 26). This study proved that the addition of Mn affects the grain size and thus has the influence on the mechanical properties of the alloys. However, the phase analysis performed using the EDS, which has indicated the amount of Mn in both phase γ'_1 and β'_1 is shown in Fig. 2(e) (point 1 and 2).

Figure 2(f) shows the XRD results of the Cu-Al-Ni SMA with and without Mn additions. As can be seen that the modified alloys (Cu-Al-Ni-0.4 wt.% Mn, Cu-Al-Ni-0.7 wt.% Mn, and Cu-Al-Ni-1 wt.% Mn) have almost the same patterns of the base alloy (Cu-Al-Ni). However, it is found that the patterns peaks were shifted toward higher angle along with variations in their shape and intensity values after the Mn addition. On the other hand, the diffraction patterns of the alloys with and without additions have confirmed the existence of two metastable phases, γ'_1 and β'_1 . The diffraction patterns of the base alloy are (122), (0018), (128), (1210), (2010), (208), (211), (040), (320), and (311), which indicate the presence of β'_1 martensite phase, while (200), (202), and (440) indicates the presence of the γ'_1 martensite phase.

When the 0.4 wt.% of Mn is added, the peaks are shifted toward higher angle, and their intensity values increased; thus, the crystallite size increased as shown in Table 4. In addition, there are two peaks observed after the addition of Mn, i.e., (211) and (320), which are associated with β'_1 phase. With

Table 2 Transformation temperature of Cu-Al-Ni SMA with and without Mn additions

Alloy	Transformation temperatures				
	A_s , K	A_f , K	M_s , K	M_f , K	T_o , K
Cu-Al-Ni	504.76	515.14	503.98	496.94	509.56
Cu-Al-Ni-0.4wt.% Mn	515	524	512.59	505.9	518.295
Cu-Al-Ni-0.7wt.% Mn	522.6	531.99	520.59	512.89	526.29
Cu-Al-Ni-1wt.% Mn	513	522	511.58	504	516.79

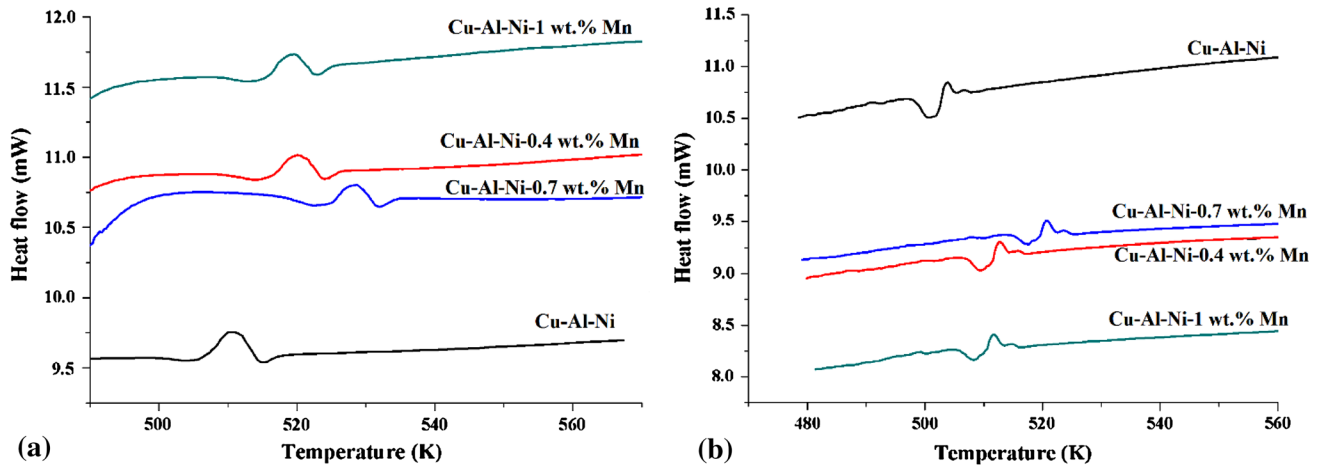


Fig. 1 DSC curves of the Cu-Al-Ni SMA with different percentage of Mn addition: (a) heating, (b) cooling

Table 3 Thermodynamic parameters of Cu-Al-Ni SMA with and without Mn additions

Alloy	$\Delta H_{\text{forward}}$, J/g	$\Delta H_{\text{reverse}}$, J/g	$\Delta S_{\text{forward}}$, J/kg K	$\Delta S_{\text{reverse}}$, J/kg K
Cu-Al-Ni	1.94	1.42	3.82	2.79
Cu-Al-Ni-0.4wt.% Mn	1.46	0.88	2.81	1.72
Cu-Al-Ni-0.7wt.% Mn	1.7	1.3	3.23	2.47
Cu-Al-Ni-1wt.% Mn	1.42	0.86	2.83	1.62

further increase of Mn percentage to 0.7 wt.%, the peaks tend to shift toward higher angle with a decrease in the intensity values; therefore, the crystallite size becomes smaller compared with Cu-Al-Ni-0.4 wt.% Mn. When the amount of Mn is increased to 1 wt.%, the peaks positions and intensities were also shifted.

The lattice parameters and crystallite size of the Cu-Al-Ni SMA with and without the addition of Mn are determined from the XRD patterns and tabulated in Table 4. The lattice parameters were evaluated in accordance with orthorhombic 18R structure in which has been proven by the XRD results. The lattice parameters were determined using the following relation (Ref 27):

$$\frac{1}{d^2} = \frac{1}{a^2} \left[\frac{h^2}{\sin^2 \beta} \right] + \frac{k^2}{b^2} + \frac{l^2}{c^2} + \left[\frac{l^2}{\sin^2 \beta} \right] - \frac{2hl \cos \beta}{ac \sin^2 \beta} \quad (\text{Eq 5})$$

The ratio of a/b is also calculated and indicated in Table 4, where this ratio for the base alloy and modified alloys is less than $\sqrt{3}/2$ in ordered case due to the atomic sizes of the constituent atoms of the 18R martensite (Ref 28, 29). The phases in XRD have a monoclinic structure depending on the obtained results, which it is similar to other works done earlier (Ref 30, 31). Although the XRD results show similar characteristics, but there are some of the diffraction peaks slightly shifted due to the addition of Mn. One of the most important factors that has a significant effect on the martensitic transformation is the structure ordering (Ref 31, 32).

In Cu-based SMA, the martensitic transformation in β -phase is evaluated according to $(110)_{\beta}$ planes of the austenite phase, which is known as a basal plane for the martensite phase (Ref 33). The basal plane in the original case has a rectangular structure with a $DO_3/L2_1$ order, and during the martensite transformation, it transforms to hexagonal structure corresponding with a hexagonal distortion (Ref 31, 33). In general,

the equilibrium phases of the Cu-Al-Ni SMA are formed from α , β , and γ phases. With alloying, some of the atomic migration may have occurred and thus would allow precipitation of any of the aforementioned phases. This diffusion processes are mainly controlled by the chemical compositions of the austenite phases and would be important for this study, since we have varied the composition of the addition element. Based on this phenomenon, the reason for phase transformation behavior variations may be explained. The crystallite size can be determined by Scherrer equation (Ref 34, 35) as follows :

$$\text{Crystallite size}(d) = \frac{0.9 * (\lambda)}{B * \cos \theta}, \quad (\text{Eq 6})$$

where λ is the XRD wavelength, β is the full width at half maximum, and θ is the Bragg's angle. However, it has been indicated that the crystallite size tends to decrease with increase the Mn addition.

Figure 3 shows the TEM images, HRTEM, and selected area diffraction of the Cu-Al-Ni SMAs with and without Mn additions. Figure 3(a) shows that the martensite is clearly formed in two morphologies; coarse variants of γ'_1 and plates groups of β'_1 , where these plates constitute from a twinned martensite laths and self-accommodation variants. Figure 3(b) shows the lattice fringes of both martensites; in addition, these fringes are oriented in different directions in accordance with the type of martensite phase. However, the analysis of the area diffraction patterns shows that the stacking sequence of the formed martensite is a monoclinic structure as shown in Fig. 3(c). When Mn is added, the morphology of the martensite phase changed, and the lattice fringes varied in term of d -spacing and orientation, and these variations can explain the occurrence of the shifting in the XRD peaks (Fig. 2f). The stacking sequence of martensite is also shown a monoclinic structure along with different positions of the peaks as indicated

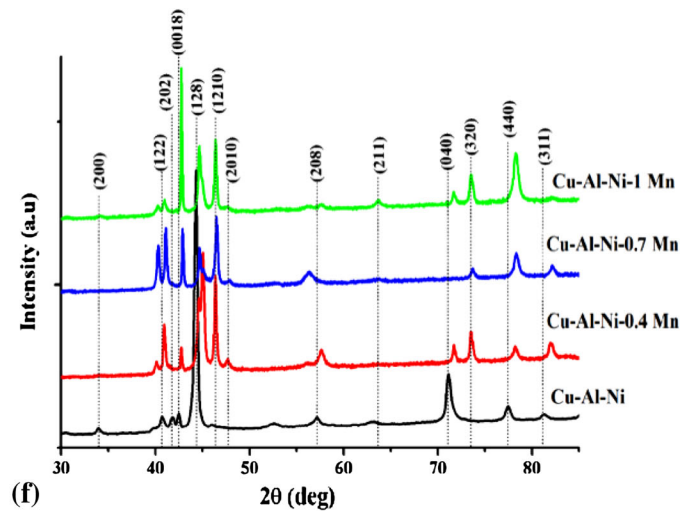
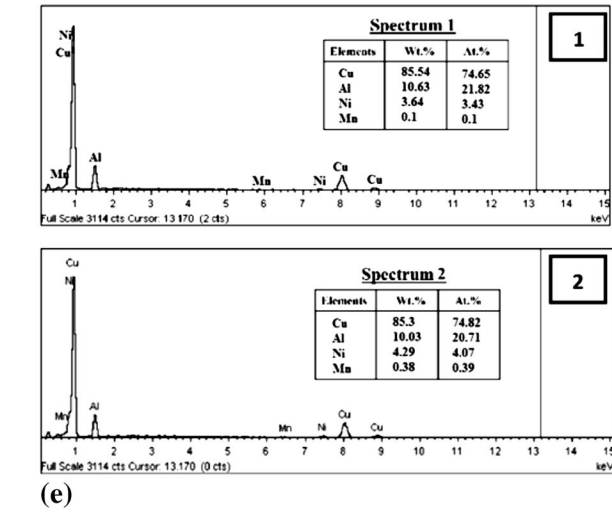
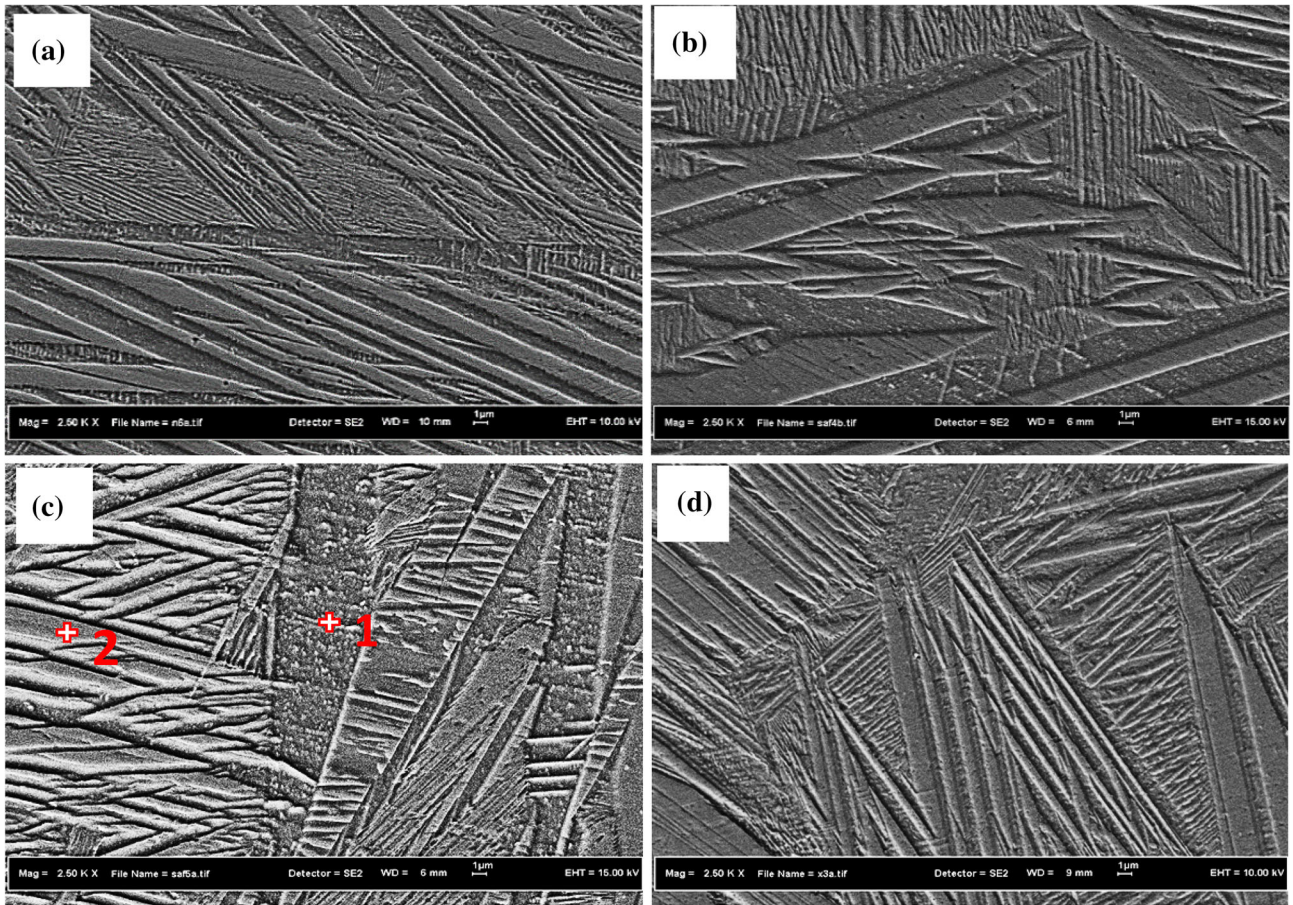


Fig. 2 FESEM micrographs of the Cu-Al-Ni SMA with different concentrations of Mn additions: (a) Cu-Al-Ni, (b) Cu-Al-Ni-0.4 wt.% Mn, (c) Cu-Al-Ni-0.7 wt.% Mn, (d) Cu-Al-Ni-1 wt.% Mn, (e) EDS analysis of the Cu-Al-Ni-0.7 wt.% Mn of Spectrum 1 and Spectrum 2, (f) x-ray diffraction pattern

Table 4 Crystallite size and lattice parameters of Cu-Al-Ni SMA with and without additions of Mn

Alloy	<i>a</i> , Å	<i>b</i> , Å	<i>c</i> , Å	<i>a/b</i>	β	Crystallite size, nm
Cu-Al-Ni	4.425	5.250	38.055	0.842	89.905	25.5
Cu-Al-Ni-0.4wt.% Mn	4.428	5.272	38.046	0.839	90.383	21.8
Cu-Al-Ni-0.7wt.% Mn	4.421	5.256	37.925	0.841	90.299	17.2
Cu-Al-Ni-1wt.% Mn	4.428	5.252	38.043	0.843	90.112	20.6

from Fig. 3(d)-(i). In addition, these peaks distributed in an orbital zone around the [000].

3.3 Mechanical Properties

3.3.1 Tensile and Hardness Test. Figure 4 shows the stress-strain curve obtained at room temperature with constant strain of 0.1 mm/min. The measured values from the stress-strain curves are given in Table 5. The Cu-Al-Ni with different percentage additions of Mn exhibited a classical feature of SMAs through obtaining a distinct elastic region followed by a linear plastic deformation region, as shown from the σ - ε curves in Fig. 4. The generation of plastic regions is mainly attributed to the induced martensite-martensite deformation region and the reorientation of the martensite detwinning/variants.

On the other hand, the fracture stress-strain of the base alloy shows a significant difference with the rest of alloys. The modified alloys show considerably higher fracture stress and strain than the base alloy; in other words, the ductility of the

alloys with the Mn additions is improved from about 1.6 to 3.6%, which is almost twice than the base alloy. The increase in ductility with the addition of the Mn element may be attributed to the significant microstructural changes and the grain refinement associated with a decrease in the degree of order of the alloys (Ref 36).

Figure 4 shows the fracture surfaces of the Cu-Al-Ni SMAs with and without the Mn additions. Base alloy exhibited a typical characteristic of brittle fractures as shown in Fig. 4(a). Cu-Al-Ni alloy with 0.4 wt.% of Mn demonstrated an intergranular fracture along with a very small transgranular fracture, as shown in Fig. 4(b). While Cu-Al-Ni alloy with 0.7 and 1 wt.% Mn alloys shows a mixed mode of transgranular and intergranular fractures, producing a significant increase in the value of ductility compared with 0.4 wt.% Mn addition, as shown in Fig. 4(c) and (d). The increase in ductility is due to the reduction in grain size which occurred after Mn additions. The fracture mode of 0.7 and 1 wt.% Mn alloys is in agreement with the behavior of the stress-strain (Fig. 4). The large grain

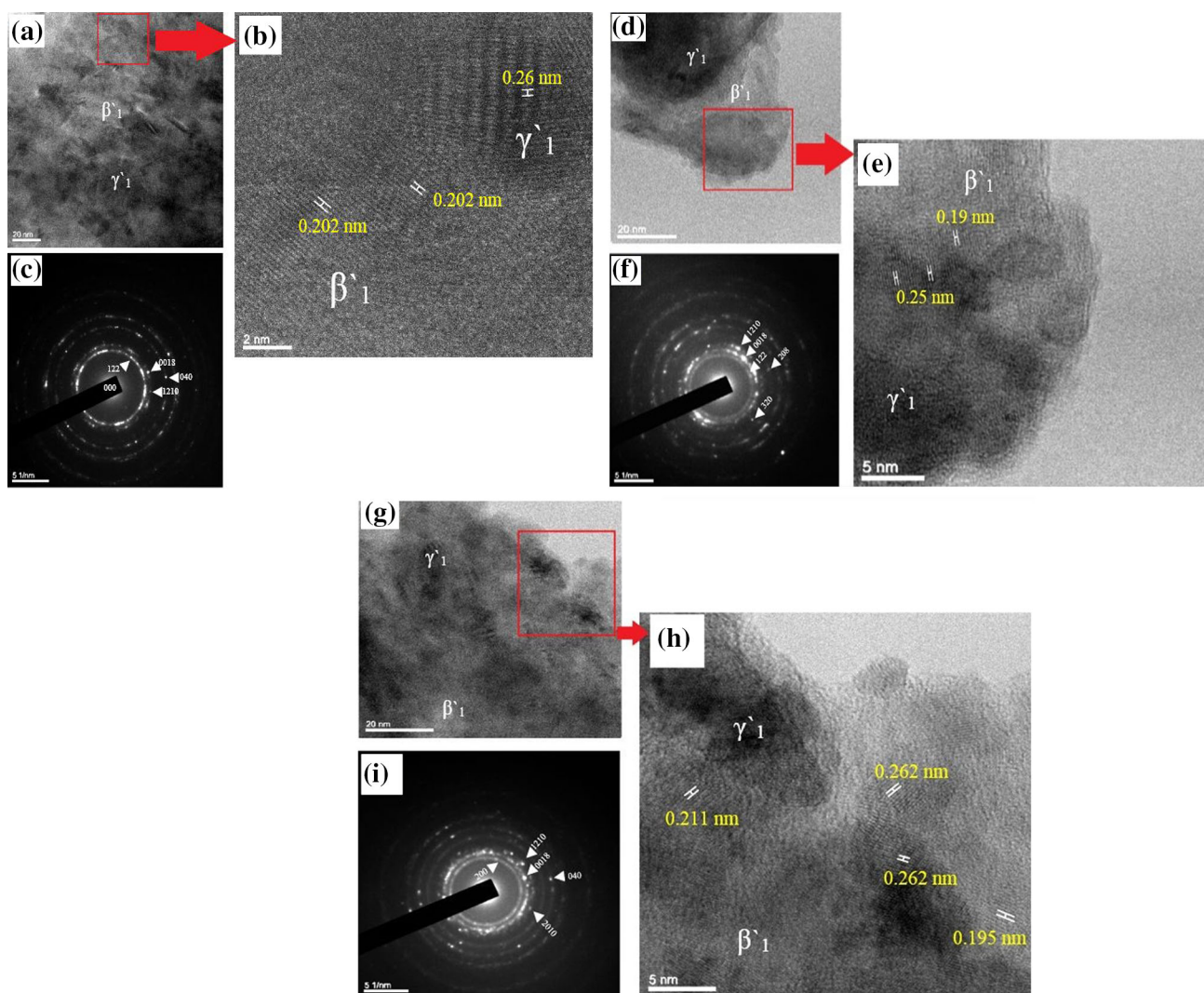


Fig. 3 TEM images corresponding with selected area diffraction patterns of Cu-Al-Ni, Cu-Al-Ni-0.7wt.% Mn, and Cu-Al-Ni-1 wt.% Mn: (a) Bright field of TEM image of Cu-Al-Ni alloy, (b) HRTEM image of the Cu-Al-Ni alloy, (c) SADP of the Cu-Al-Ni alloy, (d) Bright field of TEM image of Cu-Al-Ni-0.7Mn alloy, (e) HRTEM image of the Cu-Al-Ni-0.7 wt.% Mn alloy, (f) SADP of the Cu-Al-Ni-0.7 wt.% Mn alloy, (g) Bright field of TEM image of Cu-Al-Ni-1 wt.% Mn alloy, (h) HRTEM image of the Cu-Al-Ni-1 wt.% Mn alloy, (i) SADP of the Cu-Al-Ni-1 wt.% Mn alloy

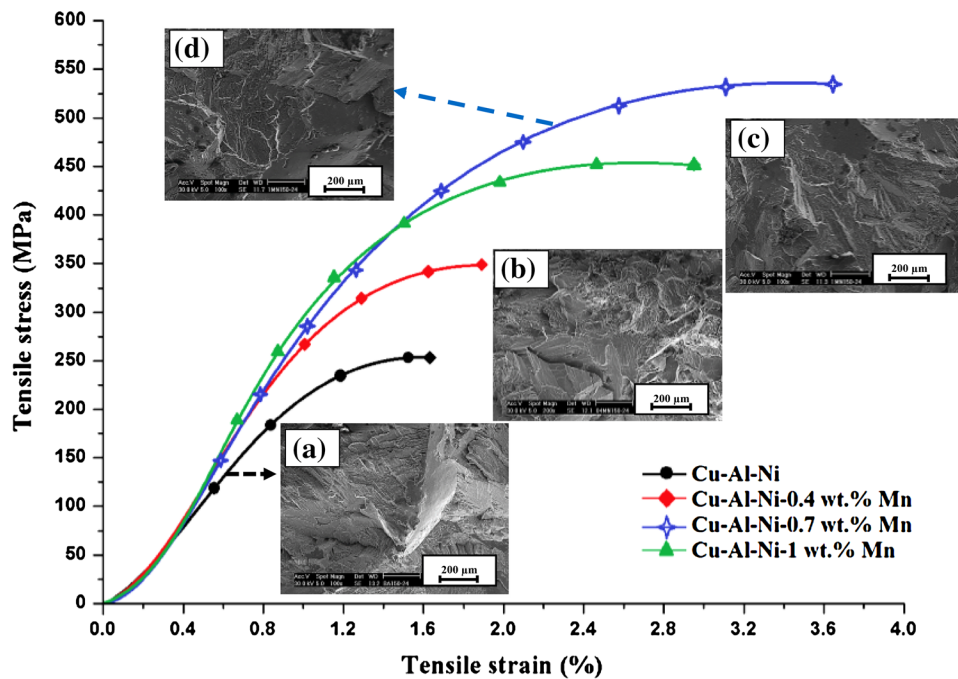


Fig. 4 Stress-strain curves obtained from the tensile test performed at room temperature along with the fracture surface of the alloys

Table 5 Results obtained from the tensile, hardness, and shape memory tests on the Cu-Al-Ni SMA with and without Mn additions

Alloy	Fracture stress (σ^F), MPa	Fracture strain (ϵ^F), %	Hardness, MPa	Strain recovery by SME (ϵ_{SME}), %
Cu-Al-Ni	270	1.6	253.6	50
Cu-Al-Ni-0.4wt.% Mn	350	2	243.4	70
Cu-Al-Ni-0.7wt.% Mn	550	3.6	210.2	90
Cu-Al-Ni-1wt.% Mn	450	3	225.4	60

size and large elastic anisotropy of Cu-Al-Ni SMA, along with difference in crystal orientations, easily increased the stress concentration at the grain and grain boundaries, thus causing a brittle fracture in the alloy. This study indicates that controlling the grain size by the addition of Mn elements will lead to reduction of the stress concentration in grain and grain boundaries, thus enhancing the ductility of the alloys. With improved ductility, the workability of these alloys can be enhanced, which can be beneficial for engineering applications. The hardness values of the Cu-Al-Ni SMAs with and without Mn additions are shown in Table 5. It was observed that different concentrations of Mn additions had a significant effect on the hardness property. As the addition of the Mn to Cu-Al-Ni SMA can lead to a decrease in grain size (Ref 21), therefore, the values of hardness are also decreased.

3.3.2 Shape Memory Effect. The strain recovery by the shape memory effect (ϵ_{SME}) of the Cu-Al-Ni SMAs with and without the Mn additions was determined by using a specially designed tensile test at $T < A_s$, whose values are given in Table 5. The ϵ_{SME} varied with the variations in the amount of Mn at the initial strain value of 1.55%, as shown in Fig. 5. It was observed that the addition of Mn with different weight percentages exhibited an increase in the values of strain recovery by the SME. Cu-Al-Ni alloy with a percentage of 0.7 wt.% Mn exhibited almost 90% of the original shape recovery after being heated to $T > A_f$. In addition, the strain

recovery increases from 50 to 90%, due to the decrease in the grain size. These enhancements in the strain recovery are attributed to the type, morphology, and orientation of the martensite phase along with the grain refinement. Furthermore, the amount of shape recovery is mainly dependent on the extent of martensitic transformation of the alloys as shown from the XRD peaks, which indicated a higher intensity of recovery after the Mn addition.

3.3.3 Electrochemical Measurements. The Potentiodynamic polarization test was performed to evaluate the corrosion behavior of Cu-Al-Ni in comparison with Cu-Al-Ni-xMn SMAs in NaCl solution (Fig. 6). It can be seen that Cu-Al-Ni SMA has more negative corrosion potential (E_{corr}) compared to Cu-Al-Ni-Mn SMAs alloy. This indicated that the addition of Mn into the Cu-Al-Ni SMA shifted E_{corr} to nobler direction and reduces the corrosion reaction of the base alloy. The results also revealed that the E_{corr} of the specimens becomes more negative, in the order of Cu-Al-Ni-0.7Mn < Cu-Al-Ni-1Mn < Cu-Al-Ni-0.4Mn < Cu-Al-Ni SMAs. The standard electrode potentials (versus SCE) of Cu, Mn, Al and Ni are 0.16 V (Cu/Cu²⁺), 1.18 V (Mn/Mn²⁺), 1.66 V (Al/Al³⁺), and 0.23 V (Ni/Ni²⁺), respectively (Ref 24). As such, Cu is the most noble of the metals, and Al is the least noble, and so the range of potentials was in the following order: Cu > Ni > Mn > Al. Therefore Al, Mn, and Ni would be more likely to electrochemically oxidize before the Cu component and resulted in the formation of the corrosion products on the

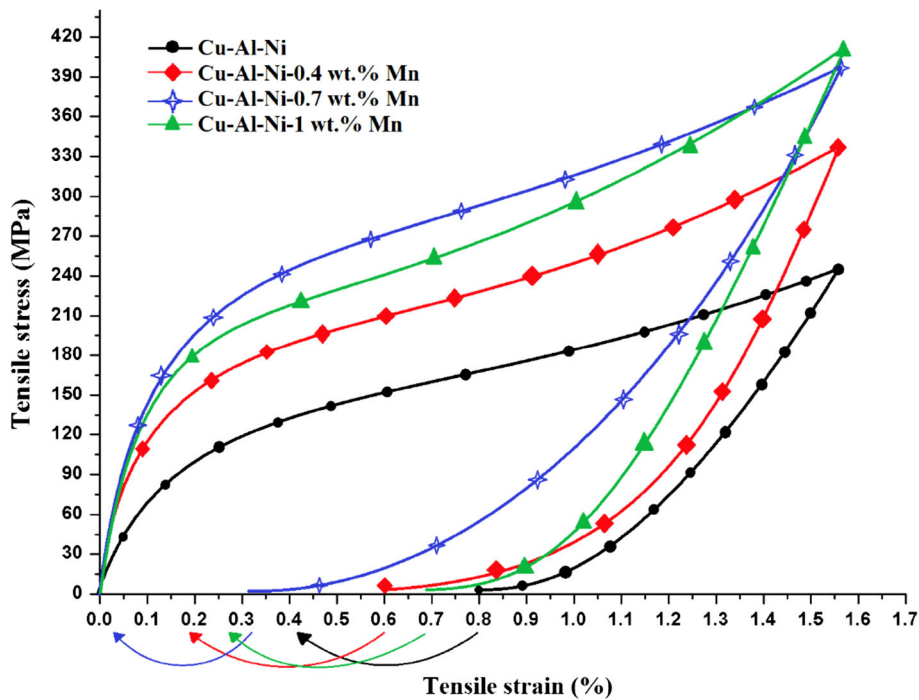


Fig. 5 Shape memory effect curves of the alloys performed at $T < A_s$, then preheated to $T > A_f$ to obtain the shape recovery

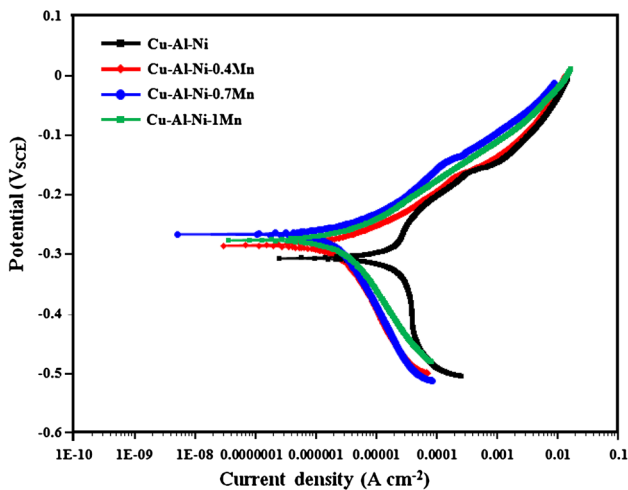


Fig. 6 Potentiodynamic polarization curves of Cu-Al-Ni and Cu-Al-Ni-Mn SMAs specimens in NaCl solution

electrode surface, which act as barrier films to protect the surface from aggressive environment and thus enhance corrosion resistance. Moreover, the presence of Mn content in the passivating film protects the SMA from the aggressive action of Cl^- better than it does in the base alloy material (Ref 37).

In this study, the addition of Mn into Cu-Al-Ni SMA leads to a reduction in grain size at all different amounts. Corrosion current density (i_{corr}) decreases from $6.93 \mu\text{A}/\text{cm}^2$ in Cu-Al-Ni to $1.43 \mu\text{A}/\text{cm}^2$ in Cu-Al-Ni-0.7Mn SMA. This can be attributed to the martensite plates and needles which are more coarsened compared to the base alloy. This is in accord with the results of Osório et al. (Ref 38) which indicating that finer martensitic structure leads to increase the galvanic corrosion effect, decreasing the general (uniform) corrosion resistance. However, this

value increased to $1.58 \mu\text{A}/\text{cm}^2$ after the addition of 1 wt.% Mn to the base alloy. This can be attributed to the appearance of a finer martensite structure which accelerates the microgalvanic corrosion and deteriorates the alloys. The corrosion current density (i_{corr}), corrosion potential (E_{corr} , V_{SCE}), cathodic Tafel slopes (β_c), anodic Tafel slopes (β_a), and corresponding corrosion rate (P_i) of specimens extracted from the polarization curves are shown in Table 6. The i_{corr} is related to the corrosion rate, P_i through the following empirical equation (Ref 39)

$$P_i = 22.85 i_{\text{corr}} \quad (\text{Eq } 7)$$

The corrosion rate of the Cu-Al-Ni SMA ($158.18 \mu\text{m}/\text{year}$) was significantly decreased after addition of the 0.7 wt.% Mn to $32.67 \mu\text{m}/\text{year}$. This is attributed to the formation of the corrosion products on the electrode surface, which act as barrier films to protect the surface from aggressive solution and thus enhanced corrosion resistance. The formation of the products such as cuprous chloride (CuCl), and cuprous oxide (Cu_2O) as well as formation of aluminum oxide/hydroxide ($\text{Al}_2\text{O}_3/\text{Al}(\text{OH})_3$) (Ref 40), and manganese oxide is the other reason of the lower corrosion current density of the Cu-Al-Ni-Mn than that of Cu-Al-Ni SMA.

Also, from the electrochemical parameters (i_{corr} , β_c and β_a) of specimens, the polarization resistance (R_p) was calculated according following equation (Ref 39):

$$R_p = \frac{\beta_a \beta_c}{2.3 (\beta_a + \beta_c) i_{\text{corr}}} \quad (\text{Eq } 8)$$

The corrosion behavior of the alloy improved as R_p values increased with the addition of Mn up to 0.7 wt.%. The addition of 0.7 wt.% of Mn into the Cu-Al-Ni SMA significantly increased the R_p from 3.82 to $16.61 \text{ k}\Omega \text{ cm}^2$. However, further addition of Mn to 1 wt.% decreases R_p value to $14.98 \text{ k}\Omega \text{ cm}^2$. The anodic Tafel slopes of the both alloys

Table 6 Electrochemical parameters of Cu-Al-Ni and Cu-Al-Ni-Mn SMAs in NaCl solution attained from the polarization test

Alloy	Corrosion potential, E_{corr} , mV vs. SCE	Current density, i_{corr} , $\mu\text{A}/\text{cm}^2$	Cathodic slope, β_C , mV/decade vs. SCE	Anodic slope β_a , mV/decade vs. SCE	Polarization resistance, R_p , $\text{k}\Omega \text{ cm}^2$	Corrosion rate, P_i , $\mu\text{m}/\text{year}$
Cu-Al-Ni	-307.4	6.93	198	88	3.82	158.18
Cu-Al-Ni-0.4Mn	-286.5	2.01	247	72	12.05	45.92
Cu-Al-Ni-0.7Mn	-267.3	1.43	256	79	16.61	32.67
Cu-Al-Ni-1Mn	-277.7	1.58	240	62	14.98	36.10

were around 75 mV/decade, which are close to the theoretical and experimental value of 60 mV/decade (Ref 41). This phenomenon indicated that the dissolution of copper to soluble CuCl_2^- ion and diffusion of soluble species from the electrode surface into bulk solution are a dominant corrosion mechanism for both alloys (Ref 40, 42). Benedett et al. (Ref 42) reported that the corrosion behavior of Cu-Al alloys was determined by aluminum dissolution accompanied with the copper dissolution. Formation of compact and protective film on the surface of Cu-Al-Ni-Mn alloy reduces the anodic dissolution rates. This protective film composed of the products such as $\text{Al}(\text{OH})_2$, $\text{Cu}_2\text{Cl}(\text{OH})_3$, and Mn-containing copper alloys contains an appreciable amount of manganese oxides or hydroxides. These oxides/hydroxides increased the surface passivity, hence improved corrosion resistance of the Cu-Al-Ni-Mn alloy compared with the base Cu-Al-Ni alloy.

4. Conclusions

The influence of Mn addition on the phase transformation behavior, mechanical properties, and corrosion characteristic of Cu-Al-Ni SMAs has been studied. The results show that with an increase in the amount of Mn addition, the grain size decreases initially and then increases. With the increase in the Mn content to 0.7 wt.%, the martensite plates and needles are coarsened and the thickness of both morphologies tends to increase. The austenite-martensite phase transformation temperatures tend to vary with the increase in Mn addition. Also, Mn addition can improve the stress-strain behavior, and shape memory effect of Cu-Al-Ni SMAs with 0.7 wt.% Mn alloy gives the highest recovery of 90% of its original shape. Polarization test showed that corrosion rates of Cu-Al-Ni-xMn alloy decreased significantly after addition of Mn with the following sequence: Cu-Al-Ni-0.7Mn < Cu-Al-Ni-1Mn < Cu-Al-Ni-0.4Mn < Cu-Al-Ni SMAs.

Acknowledgments

The author(s) would like to thank the Malaysian Ministry of Higher Education (MOHE) and Universiti Teknologi Malaysia for providing the financial support and facilities for this research, under Grant No. R.J130000.7824.4F150.

References

- O. Benafan, A. Garg, R.D. Noebe, G.S. Bigelow, S.A. Padula II, D.J. Gaydos, N. Schell, J.H. Mabe, and R. Vaidyanathan, Mechanical and Functional Behavior of a Ni-rich Ni_{50.3}Ti_{29.7}Hf₂₀ High Temperature Shape Memory Alloy, *Intermetallics*, 2014, **50**, p 94–107

- A. Ibarra, J.S. Juan, E.H. Bocanegra, and M.L. Nó, Thermo-mechanical Characterization of Cu-Al-Ni Shape Memory Alloys Elaborated by Powder Metallurgy, *Mater. Sci. Eng. A*, 2006, **438–440**, p 782–786
- I.H.V. Recarte, J. Herreros, M.L. No, and J. San Juan, Precipitation of the Stable Phases in Cu-Al-Ni Shape Memory Alloys, *Scripta Mater.*, 1996, **34**, p 255–260
- R.B. Pérez-Sáez, V. Recarte, E.H. Bocanegra, M.L. No, and J. San Juan, Dependence of the Martensitic Transformation Characteristics on Concentration in Cu-Al-Ni Shape Memory Alloys, *Mater. Sci. Eng. A*, 1999, **273–275**, p 380–384
- V. Recarte, J.I. Pérez-Landazábal, M.L. Nó, and J. San Juan, Study by Resonant Ultrasound Spectroscopy of the Elastic Constants of the β Phase in Cu-Al-Ni Shape Memory Alloys, *Mater. Sci. Eng. A*, 2004, **370**, p 488–491
- J. Font, E. Cesari, J. Muntasell, and J. Pons, Thermomechanical Cycling in Cu-Al-Ni-Based Melt-Spun Shape-Memory Ribbons, *Mater. Sci. Eng. A*, 2003, **354**, p 207–211
- J.I. Pérez-Landazábal, V. Recarte, V. Sánchez-Alarcos, M.L. Nó, and J.S. Juan, Study of the Stability and Decomposition Process of the β Phase in Cu-Al-Ni Shape Memory Alloys, *Mater. Sci. Eng. A*, 2006, **438–440**, p 734–737
- T. Saburi and C.M. Wayman, Crystallographic Similarities in Shape Memory Martensites, *Acta Metall.*, 1979, **27**, p 979–995
- J.I. Pérez-Landazábal, V. Recarte, M.L. Nó, and J. San Juan, Determination of the Order in γ_1 Intermetallic Phase in Cu-Al-Ni Shape Memory Alloys, *Intermetallics*, 2003, **11**, p 927–930
- U. San and İ. Aksoy, Electron Microscopy Study of 2H and 18R Martensites in Cu-11.92 wt.% Al-3.78 wt.% Ni Shape Memory Alloy, *J. Alloy. Compd.*, 2006, **417**, p 138–142
- H.S.S. Sugimoto, T. Hara, and H. Tsuchiya, The Effect of Grain Constraint, Heat Treatment and Compositional Change on the Behavior of Martensitic Transformations in Alloys with the Composition Near Cu-13Al-4Ni-1Zn (mass%), *J. Phys. IV*, 1995, **5**, p 925
- V. Recarte, R.B. Pérez-Sáez, J. SanJuan, E.H. Bocanegra, and M.L. Nó, Influence of Al and Ni Concentration on the Martensitic Transformation in Cu-Al-Ni Shape-Memory Alloys, *Metall. Mater. Trans. A*, 2002, **33**, p 2581–2591
- H.Y. Peng, Z.G. Wei, D.Z. Yang, C.Y. Chung, and J.K.L. Lai, Reverse Transformations in CuAlNiMnTi Alloy at Elevated Temperatures, *Acta Mater.*, 1996, **44**, p 1189–1199
- M.A. Morris, Microstructural Influence on Ductility and Shape Memory Effect of Some Modified Cu-Ni-Ai Alloys, *Scripta Metall.*, 1991, **25**, p 1409–1414
- M.A. Morris and S. Gunter, Effect of Heat Treatment and Thermal Cycling on Transformation Temperatures of Ductile Cu-Al-Ni-Mn-B Alloys, *Scripta Metall. Mater.*, 1992, **26**(11), p 1663–1668
- M.A. Morris and T. Lipe, Microstructural Influence of Mn Additions on Thermoelastic and Pseudoelastic Properties of Cu-Al-Ni Alloys, *Acta Metall. Mater.*, 1994, **42**, p 1583–1594
- U. San and T. Kırındı, Effects of Deformation on Microstructure and Mechanical Properties of a Cu-Al-Ni Shape Memory Alloy, *Mater. Charact.*, 2008, **59**, p 920–929
- J. Rodríguez-Aseguinolaza, I. Ruiz-Larrea, M.L. Nó, A. López-Echarri, E.H. Bocanegra, and J. San Juan, Thermal History Effects of Cu-Al-Ni Shape Memory Alloys Powder Particles Compared with Single Crystals Behaviour, *Intermetallics*, 2010, **18**, p 2183–2190
- Y. Sutou, T. Omori, K. Yamauchi, N. Ono, R. Kainuma, and K. Ishida, Effect of Grain Size and Texture on Pseudoelasticity in Cu-Al-Mn-Based Shape Memory Wire, *Acta Mater.*, 2005, **53**, p 4121–4133

20. K. Adachi, K. Shoji, and Y. Hamada, Formation of (X) Phases and Origin of Grain Refinement Effect in Cu-Al-Ni Shape Memory Alloys Added with Titanium, *ISIJ Int.*, 1989, **29**, p 378–387
21. U. Sari, Influences of 2.5 wt.% Mn Addition on the Microstructure and Mechanical Properties of Cu-Al-Ni Shape Memory Alloys, *Int. J. Miner. Metall. Mater.*, 2010, **17**, p 192–198
22. S.H. Chang, Influence of Chemical Composition on the Damping Characteristics of Cu-Al-Ni Shape Memory Alloys, *Mater. Chem. Phys.*, 2011, **125**, p 358–363
23. A. Sudholz, K. Gusieva, X. Chen, B. Muddle, M. Gibson, and N. Birbilis, Electrochemical Behaviour and Corrosion of Mg-Y Alloys, *Corros. Sci.*, 2011, **53**, p 2277–2282
24. C. Tatar, Gamma Irradiation-Induced Evolution of the Transformation Temperatures and Thermodynamic Parameters in a CuZnAl Shape Memory Alloy, *Thermochim. Acta*, 2005, **437**, p 121–125
25. J. Ortín and A. Planes, Thermodynamics of Thermoelastic Martensitic Transformations, *Acta Metall.*, 1989, **37**, p 1433–1441
26. H. Funakubo, *Shape Memory Alloys*, CRC Press LLC, Boca Raton, 1987
27. J.B.Q. Xuan and T.Y. Hsu, The Effect of Martensite Ordering on Shape Memory Effect in a Copper-Zinc-Aluminium Alloy, *Mater. Sci. Eng.*, 1987, **93**, p 205–211
28. R.J. Salzbrenner and M. Cohen, On the Thermodynamics of Thermoelastic Martensitic Transformations, *Acta Metall.*, 1979, **27**, p 739–748
29. O. Adigüzel, Martensite Ordering and Stabilization in Copper Based Shape Memory Alloys, *Mater. Res. Bull.*, 1995, **30**, p 755–760
30. V. Sampath, Studies on the Effect of Grain Refinement and Thermal Processing on Shape Memory Characteristics of Cu-Al-Ni Alloys, *Smart Mater. Struct.*, 2005, **14**, p S253–S260
31. Ş.N. Balo and N. Sel, Effects of Thermal Aging on Transformation Temperatures and Some Physical Parameters of Cu-13.5wt.%Al-4wt.%Ni Shape Memory Alloy, *Thermochim. Acta*, 2012, **536**, p 1–5
32. G.-S. Yang, J.-K. Lee, and W.-Y. Jang, Effect of Grain Refinement on Phase Transformation Behavior and Mechanical Properties of Cu-Based Alloy, *Trans. Nonferrous Met. Soc. China*, 2009, **19**, p 979–983
33. A. Aydogdu, Y. Aydogdu, and O. Adiguzel, Long-Term Ageing Behaviour of Martensite in Shape Memory Cu-Al-Ni Alloys, *J. Mater. Process. Technol.*, 2004, **153–154**, p 164–169
34. B.D. Cullity and S.R. Stock, *Elements of x-ray diffraction*, Prentice Hall, Upper Saddle River, 2001
35. A.L. Patterson, The Scherrer Formula for x-ray Particle Size Determination, *Phys. Rev.*, 1939, **56**, p 978–982
36. U.S. Mallik and V. Sampath, Influence of Aluminum and Manganese Concentration on the Shape Memory Characteristics of Cu-Al-Mn Shape Memory Alloys, *J. Alloy. Compd.*, 2008, **459**, p 142–147
37. M. Pisarek, P. Kędzierzawski, T. Płociński, M. Janik-Czachor, and K.J. Kurzydłowski, Characterization of the Effects of Hydrostatic Extrusion on Grain Size, Surface Composition and the Corrosion Resistance of Austenitic Stainless Steels, *Mater. Charact.*, 2008, **59**, p 1292–1300
38. W.R. Osório, A. Cremasco, P.N. Andrade, A. Garcia, and R. Caram, Electrochemical Behavior of Centrifuged Cast and Heat Treated Ti-Cu Alloys for Medical Applications, *Electrochim. Acta*, 2010, **55**, p 759–770
39. H. Bakhsheshi-Rad, M. Idris, and M. Abdul-Kadir, Synthesis and In Vitro Degradation Evaluation of the Nano-HA/MgF₂ and DCPD/MgF₂ Composite Coating on Biodegradable Mg-Ca-Zn Alloy, *Surf. Coat. Technol.*, 2013, **222**, p 79–89
40. M. Gojić, L. Vrsalović, S. Kožuh, A. Kneissl, I. Anžel, S. Gudić, B. Kosec, and M. Kliškic, Electrochemical and Microstructural Study of Cu-Al-Ni Shape Memory Alloy, *J. Alloy. Compd.*, 2011, **509**, p 9782–9790
41. S. Montecinos and S.N. Simison, Influence of the Microstructure on the Corrosion Behaviour of a Shape Memory Cu-Al-Be Alloy in a Marine Environment, *Appl. Surf. Sci.*, 2011, **257**, p 2737–2744
42. A. Benedetti, P. Sumodjo, K. Nobe, P. Cabot, and W. Proud, Electrochemical Studies of Copper, Copper-Aluminium and Copper-Aluminium-Silver Alloys: Impedance Results in 0.5 M NaCl, *Electrochim. Acta*, 1995, **40**, p 2657–2668